The Astronomical Journal, 160:71 (9pp), 2020 August https://doi.org/10.3847/1538-3881/ab9d88

Using the Baryonic Tully–Fisher Relation to Measure H_o

James Schombert[1], Stacy McGaugh[2], and Federico Lelli[3]
[1] Institute for Fundamental Science, University of Oregon, Eugene, OR 97403, USA
[2] Department of Astronomy, Case Western Reserve University, Cleveland, OH 44106, USA
[3] School of Physics and Astronomy, Cardiff University, Queens Buildings, The Parade, Cardiff, CF24 3AA, UK
Received 2020 May 3; revised 2020 June 11; accepted 2020 June 15; published 2020 July 17

Abstract

We explore the use of the baryonic Tully–Fisher relation (bTFR) as a new distance indicator. Advances in near-IR imaging and stellar population models, plus precise rotation curves, have reduced the scatter in the bTFR such that distance is the dominant source of uncertainty. Using 50 galaxies with accurate distances from Cepheids or the tip magnitude of the red giant branch, we calibrate the bTFR on a scale independent of H_o. We then apply this calibrated bTFR to 95 independent galaxies from the SPARC sample, using CosmicFlows-3 velocities, to deduce the local value of H_o. We find $H_o = 75.1 \pm 2.3$ (stat) ± 1.5 (sys) km s^{-1} Mpc^{-1}.

Unified Astronomy Thesaurus concepts: Cosmology (343); Hubble constant (758)

1. Introduction

The classic Tully–Fisher (TF) relation links the rotation velocity of a disk galaxy to its stellar mass and/or luminosity in a given photometric band. Because the observed rotation velocities do not depend on galaxy distance D, while stellar luminosities depend on D^2, the TF relation is a key distance indicator that has played a crucial and historical role in constraining the value of H_o (see Tully & Fisher 1977; Sakai et al. 2000). The classic TF relation, however, breaks down at stellar masses below approximately $10^9\,M_\odot$, when dwarf galaxies in groups and in the field environment become progressively more gas rich. By replacing the stellar mass with the total baryonic mass (stars plus gas, M_b), one recovers a single linear relation: the so-called baryonic Tully–Fisher relation (bTFR; Freeman 1999; McGaugh et al. 2000; Verheijen 2001; Zaritsky et al. 2014).

The bTFR samples deeper into the galaxy mass function, as low-mass dwarfs typically have high gas fractions and the neutral gas can constitute 80%–90% of the total baryonic mass (Bradford et al. 2015). This results in a large amount of scatter in the classic TF relation with a corresponding loss in accuracy as a distance indicator, which is eliminated by including the gas mass. Currently, the bTFR extends over two decades in velocity and six decades in M_b (McGaugh 2012; Iorio et al. 2017). Moreover, it displays a surprisingly small scatter, considering the number of possible competing astrophysical processes that produce this relation (Lelli et al. 2016a).

The bTFR combines rotational velocity (V) and baryon mass (M_b) in the form of $M_b = AV^x$ that, unlike most astrophysical correlations, does not show any room for a third parameter such as characteristic radius or surface brightness (Lelli et al. 2019). In a log–log bTFR plot, x becomes the slope of the relationship, and log A becomes the zero point. As V is distance independent, errors in distance only reflect into M_b (going as D^2). While the scatter in the bTFR can be used to constrain galaxy formation models in a ΛCDM cosmology (Dutton 2012), it also presents a unique opportunity to test the consistency of the distance scale zero point (i.e., H_o) with redshift-independent calibrators of the bTFR.

A new local test of H_o has become critical, for over the past decade there have been growing discrepancies in the determination of H_o by different methods. On one hand, the Cepheid (C) calibration to Type Ia supernovae (SNe Ia) yields $H_o = 73.2 \pm 1.7$ km s^{-1} Mpc^{-1} (Riess et al. 2016). Using the tip of the red giant branch (TRGB) method to calibrate the SN distance scale yields a slightly lower $H_o = 69.8 \pm 0.8$ km s^{-1} Mpc^{-1} (Freedman et al. 2019). However, fitting the angular power spectrum of cosmic microwave background (CMB) fluctuations in the Planck data with ΛCDM models produces a value of H_o of 67.4 ± 0.5 (Planck Collaboration et al. 2016). In addition, an H_o value of 67.3 ± 1.1 was found from the SDSS-III Baryon Oscillation Spectroscopic Survey (BOSS) measurements of the baryon acoustic oscillations (Aubourg et al. 2015). Both of these measurements, which hinge on a ΛCDM-driven interpretation of the CMB, represent a 6σ difference from the Cepheid-calibrated SN distance scale (Verde et al. 2019).

In this paper, we present a redshift-independent calibration of the bTFR using galaxies with Cepheid and TRGB distances (see Sorce et al. 2013) from a subset of the Spitzer Photometry and Accurate Rotation Curves (SPARC) sample and of Ponomareva et al. (2018). This baseline bTFR is then compared to the larger SPARC data set with new CosmicFlows-3 velocities (Tully et al. 2019) to examine variations in the bTFR normalization for different H_o values.

2. Data

2.1. The SPARC Galaxy Database

The SPARC data set consists of H I rotation curves (RC) accumulated over the last three decades of radio interferometry combined with deep near-IR photometry from the Spitzer 3.6 μm IRAC camera (Lelli et al. 2016b). This provides the community an important combination of extended H I rotation curves (mapping the galaxy gravitational potential out to large radii) plus near-IR surface photometry to map the stellar component (see also Zaritsky et al. 2014). In addition, the H I observations also provide the H I gas mass that, when corrected for small amounts of He and heavier elements, becomes the total gas mass of a galaxy.

The SPARC sample spans a broad range in baryonic mass (10^8–$10^{11}\,M_\odot$), surface brightness (3–1000 $L_\odot$ pc^{-2}), and rotation velocity (V_f from 20 to 300 km s^{-1}). The SPARC data set also contains every Hubble late type producing a representative sample of disk galaxies from dwarf irregulars

to massive spirals with large bulges. The details of the sample are listed in Lelli et al. (2016b) and the resulting science outlined in McGaugh et al. (2016). The SPARC sample and analysis with respect to the bTFR are presented in Lelli et al. (2016a). The analysis presented herein follows that paper with respect to error analysis plus small additions and corrections to the data as outlined in Lelli et al. (2019).

For sample selection, we have isolated a subset of 125 galaxies that follow the quality criterion outlined in Lelli et al. (2019) plus two additional galaxies with good TRGB distances. That study examined 153 objects in the original sample, excluding 22 galaxies with low inclinations ($i < 30°$) where geometric corrections are uncertain, and another six galaxies with low-quality rotation curves that do not appear to track the equilibrium gravitational potential of the system. As discussed in Lelli et al. (2019), the average circular velocity along the flat portion of the rotation curve (V_f) results in the tightest correlation between rotation and total baryonic mass (see their Figure 2). This measure of rotation velocity is superior to single-dish measures (such as W_{P20} or W_{M50}) or velocities based on some disk scale length (e.g., V_{2R_e}) or peak of the rotation curve. Only those rotation curves that display a flat outer portion (neither rising or falling) were included in the sample, and it is those values (V_f) that will form one axis of the bTFR for our analysis.

The other axis of the bTFR is total baryonic mass, the sum of all of the observed components, stars and gas ($M_b = M_* + M_g$). Of the two components to the baryonic mass, the stellar component has the highest uncertainty as it is determined by measuring a luminosity at a specific wavelength multiplied by the appropriate mass-to-light ratio (Υ_*) for that wavelength. The mass-to-light ratio is obtained from stellar population models (e.g., Bell et al. 2003; Portinari et al. 2004; Meidt et al. 2014; Schombert et al. 2019) considering the galaxy color to account for the effects of star formation. The physics of star formation, and later stellar evolution, are such that the Υ_* deduced from optical luminosities are highly sensitive to the galaxy's star formation rate (SFR) and produce uncertain stellar masses. Values in the near-IR are less sensitive to a galaxy's star formation history and have the additional advantage of minimizing absorption by dust. For this analysis, we use the Υ_* values obtained from Schombert et al. (2019) of 0.5 for disk regions and 0.7 for bulge regions at the IRAC channel 1 wavelength of 3.6 μm. We use fits to the Spitzer 3.6 surface brightness profiles to determine a galaxy's bulge-to-disk ratio (B/D) and apply the appropriate Υ_* to the luminosities of those components.

The SPARC sample pays extra attention to gas-rich, low-surface-brightness (LSB) galaxies that typically populate the low-mass end of the bTFR. Unlike the luminous TF relation (Tully et al. 2013), the galaxies on the low-mass end are dominated by a gas component, and simply using the galaxy luminosity as a proxy for baryonic mass is inaccurate. Fortunately, the same H I observations that yield the rotation velocity, V_f, also provide detailed information about the gas content. In particular, neutral atomic (H I) gas dominates the gas component in typical star-forming galaxies and, therefore, the gas mass can be deduced directly from the physics of the spin–flip transition of hydrogen times the cosmic hydrogen fraction plus minor corrections for molecular hydrogen and heavier elements. While the contribution of ionized gas is considered in numerical simulations (Gnedin 2012), we found no evidence of large amounts of diffuse Hα emission or X-ray output in the gas-rich galaxies of our sample (Schombert et al. 2011; Qu & Bregman 2019) where such a correction would dominate.

2.2. Uncertainties

Aside from distance errors, errors to the baryon mass have four components: (1) errors in the 3.6 photometry, (2) errors in the H I fluxes, (3) uncertainty in the conversion of near-IR luminosity to stellar mass (Υ_*), and (4) uncertainty in the conversion of atomic gas mass into total gas mass. The first two are due to errors in the observations and are outlined in Lelli et al. (2016b). These error estimates are substantiated by comparison to 2MASS K-band photometry and other H I studies (Schombert & McGaugh 2014). They are typically of the order of 3% for the 3.6 luminosities and 10% for H I fluxes, which translate into a mean error of 0.04 in log M_b.

The second set of errors are systematic to assumptions in the conversion of the observed values to mass values. For example, systematic errors in the modeling of Υ_* are explored in Schombert et al. (2019), where scenarios with different assumptions on the star formation history or the stellar mass function produced different relationships between color and Υ_*. However, there are only a limited number of stellar population models that also reproduce the main-sequence diagrams (the correlation of stellar mass versus star formation rate which indicate nearly constant SF over a Hubble time for most of the SPARC sample) and the distribution of colors from the UV to near-IR (see Schombert et al. 2019). Those models are well approximated by using a singular value of 0.5 for Υ_* in the disk regions and a value of 0.7 for bulges.

Through the use of Bayesian rotation-curve fits with dark matter halos, the plausible galaxy-to-galaxy variations of Υ_* can be explored (Li et al. 2020). From those simulations, we find that the Υ_* at 3.6 μm for the blue colors typical of low-mass galaxies span a range from 0.45 to 0.60. This is in agreement with the possible range of Υ_* from stellar population models given the range in galaxy colors. For early-type galaxies with large bulges, the value of Υ_* can range from 0.6 to 0.7. Thus, the systematic variation for Υ_* is approximately 0.15 for disks and 0.10 for bulges.

Likewise, the gas correction term to convert H I values into total gas mass has two components of uncertainty, metallicity and the amount of molecular gas in a galaxy. In the past, we have used a conversion factor (η) of 1.33 for atomic to total gas mass that corrects for the abundance of He in low-metallicity systems (high-mass disks have metallicities near solar, but their gas fractions are small; see McGaugh 2012). We have also ignored molecular gas (primarily H_2) owing to the arguments outlined in McGaugh (2012) and observations from McGaugh & Schombert (2015).

In this paper, we will make minor corrections for metallicity and molecular gas using scaling relations from McGaugh et al. (2020). The gas metallicity causes the gas correction term, η, to vary from 1.33 for low-metallicity systems to 1.40 for galaxies with metallicity near solar (McGaugh 2012). As the gas-rich systems in our study are typically low in stellar mass, their metallicities are expected to be low. In comparison, the high-metallicity galaxies have high η values but their gas component is small. For this study, we allow η to vary with mass/metallicity

Table 1
Systematic Error Budget

Case	log A	x	ΔH_o	Notes
Baseline	1.79 ± 0.34	3.95 ± 0.16	⋯	50 C/TRGB galaxies
Low Υ_*	1.86 ± 0.24	3.90 ± 0.11	−0.4	$\Upsilon_* = 0.4$
High Υ_*	1.63 ± 0.24	4.02 ± 0.11	+0.2	$\Upsilon_* = 0.6$
No molecules	1.80 ± 0.24	3.93 ± 0.11	−0.3	
No heavy elements	1.74 ± 0.24	3.96 ± 0.11	+0.1	$\eta = 1.33$
High TRGB zero point	1.81 ± 0.33	3.94 ± 0.16	+0.3	+0.05 mag
Low TRGB zero point	1.77 ± 0.34	3.96 ± 0.16	−0.3	−0.05 mag

Note. The bTFR is in the form of $M_b = AV_f^x$.

following the prescriptions in McGaugh et al. (2020); however, this correction is small (see Table 1).

A similar correction is needed for the contribution of molecular gas, which again is measured to be very low for low-mass galaxies and higher for high-mass systems. From studies of H_2 content in disk galaxies, we adopt a scaling relation from total stellar mass to M_{H_2} (McGaugh et al. 2020). The contribution of H_2 varies from 1% to 8% with a mean of 5% for the SPARC sample. This is at the same level as the variation in η for the combined gas content.

To quantify the magnitude of the above variations on the baryon mass, we have listed six scenarios in Table 1. Here we have made a maximum likelihood fit (Lelli et al. 2019) using the BayesLineFit software.[4] We fit both the baseline sample of 50 galaxies with Cepheid and TRGB distances and adequate V_f values (this sample is described in greater detail in Section 2.3) and the SPARC sample (assuming an $H_o = 75\ \mathrm{km\ s^{-1}\ Mpc^{-1}}$ for illustration). We then alter the prescriptions used to calculate the baryonic mass in the six different ways listed in Table 1 and recalculate the maximum likelihood fit.

The largest uncertainty from the stellar population model assumptions arises from varying Υ_*, although the variations in metallicity or molecules for the gas mass are of the same order of magnitude. More importantly, neither corrections to stellar or gas mass have a significant influence on the deduced slope of the bTFR. All the slopes are well within the errors of the fitted slope of the redshift-independent sample of 3.95 ± 0.16. For example, a change in η due to metallicity changes the slope of the main sample by only 0.05. Large variations in the slope of the bTFR would make a skewed distribution of residuals from the bTFR, key to deducing an H_o for each subsample.

In addition, any change in the zero point (a shift of the baryon mass to higher or lower values due to systematic changes in Υ_* or η) has no effect on the use of the bTFR as a distance indicator as those shifts are made to the calibrating galaxies as well as the main sample in identical ways. Because the calibrating Cepheid and TRGB sample also covers the same mass range as the full sample, any minor changes in the slope would also have a negligible effect on the estimate of H_o.

We also list in Table 1 the very small uncertainty due to a zero-point correction to the TRGB distance scale (46% of the calibrating sample) from the discussion in Freedman et al. (2019). A larger systematic shift in the TRGB zero point would imply a major offset between Cepheids and TRGB calibrator galaxies in the bTFR plane, which appears unphysical. This zero-point error is the smallest of all of the systematic corrections. The uncertainty in using just TRGB (23 galaxies) or Cepheid (27 galaxies) calibrators is also small. As the Cepheid calibrators are primarily high in mass, this produces a shallower slope to the bTFR ($x = 3.70$) compared to the entire sample. However, this is still within the errors of all of the other subsamples and is mitigated by the inclusion of a larger dynamic range for the SPARC bTFR.

Errors in V_f are independent of distance, only constrained by the errors in the H I measurements themselves. The uncertainty in V_f considers three sources of error: (1) the random error on each velocity point along the flat part of the rotation curve, quantifying noncircular motions and kinematic asymmetries between the two sides of the disk, (2) the dispersion around the estimate of V_f along the rotation curve, quantifying the actual degree of flatness, and (3) the assumed inclination angle, which is generally derived from fitting the H I velocity field. Quantifying the degree of flatness of the rotation curve and the error of the outer disk inclination is outlined in Lelli et al. (2016b), and new error calculations are presented in Lelli et al. (2019) with a mean of 8% for the sample. This translates into a mean error of 0.02 in log V_f on the x-axis of the bTFR.

2.3. Distances

Distance is the critical parameter for converting 3.6 apparent magnitudes and H I fluxes into stellar and gas masses (as both are dependent on D^2) and, thereby, into total baryonic masses (M_b). Within our 125 SPARC galaxies with accurate RCs, there are 30 galaxies with redshift-independent Cepheid or TRGB distances. The Cepheid and TRGB galaxies are listed in Table 2 (TRGB distances and errors are from Tully et al. 2019; Cepheid distances and errors are from Bhardwaj et al. 2016).

In addition to the SPARC sample, we have also considered 20 intermediate-mass disk galaxies from the Ponomareva et al. (2018) study, which also has Cepheid or TRGB distances (listed in Table 3). Of the 31 galaxies in the Ponomareva et al. sample that met our inclination and accurate RC criterion, 11 are already in the SPARC sample and we have used the SPARC data. For the remaining 20 galaxies, we have used their published H I fluxes and V_f values, but have redetermined their stellar mass values using our own Spitzer 3.6 luminosities, plus our adopted Υ_* values and gas mass prescriptions. Their quoted errors are similar to the SPARC sample. The final sample of 50 galaxies is show in Figure 1 and is used to calibrate the bTFR with galaxies having redshift-independent distances (hereafter, the C/TRGB sample). For uniformity, we only used the distances from Tully et al. (2019) and Bhardwaj et al. (2016) for both the SPARC and Ponomareva et al. samples.

To check the internal consistency in the Cepheid versus TRGB methods, there are 41 galaxies in the CosmicFlows-3 database with both Cepheid distances and TRGB measurements. Comparison between these Cepheid and TRGB distances indicates an internal dispersion of 2% in distance with no obvious systematics (although there are very few galaxies with C/TRGB distances beyond 10 Mpc). As discussed in Freedman et al. (2019), the error in the C/TRGB zero point is, at most, 0.05 mag (2% in distance), which is consistent with the dispersion between the Cepheid and TRGB methods from the CosmicFlows-3 data set.

[4] BayesLineFit is available at http://astroweb.cwru.edu/SPARC/.

Table 2
SPARC Cepheids/TRGB Calibrating Galaxies

Galaxy	D (Mpc)	log V_f (km s^{-1})	log M_b ($M_\odot$)	Distance Method
D631-7	7.87 ± 0.20	1.76 ± 0.03	8.71 ± 0.05	TRGB
DDO154	4.04 ± 0.15	1.67 ± 0.02	8.60 ± 0.06	TRGB
DDO168	4.25 ± 0.20	1.73 ± 0.03	8.82 ± 0.06	TRGB
IC 2574	3.89 ± 0.14	1.82 ± 0.04	9.29 ± 0.06	TRGB
NGC 0024	7.67 ± 0.32	2.03 ± 0.03	9.53 ± 0.09	TRGB
NGC 0055	1.89 ± 0.05	1.93 ± 0.03	9.57 ± 0.08	Cepheids
NGC 0247	3.41 ± 0.14	2.02 ± 0.04	9.73 ± 0.08	Cepheids
NGC 0300	1.91 ± 0.06	1.97 ± 0.08	9.38 ± 0.08	Cepheids
NGC 0891	9.12 ± 0.34	2.33 ± 0.01	10.86 ± 0.11	TRGB
NGC 1705	5.51 ± 0.20	1.86 ± 0.03	8.65 ± 0.11	TRGB
NGC 2366	3.34 ± 0.09	1.70 ± 0.03	9.02 ± 0.11	Cepheids
NGC 2403	3.18 ± 0.09	2.12 ± 0.02	9.99 ± 0.08	Cepheids
NGC 2683	8.59 ± 0.36	2.19 ± 0.03	10.56 ± 0.11	TRGB
NGC 2841	14.60 ± 0.47	2.45 ± 0.02	11.13 ± 0.13	Cepheids
NGC 2915	4.29 ± 0.20	1.92 ± 0.04	9.06 ± 0.06	TRGB
NGC 2976	3.63 ± 0.13	1.93 ± 0.05	9.33 ± 0.11	TRGB
NGC 3109	1.30 ± 0.03	1.82 ± 0.02	8.85 ± 0.06	Cepheids
NGC 3198	13.40 ± 0.55	2.18 ± 0.01	10.53 ± 0.11	Cepheids
NGC 3741	3.23 ± 0.12	1.70 ± 0.03	8.42 ± 0.06	TRGB
NGC 3972	20.80 ± 0.67	2.12 ± 0.02	10.10 ± 0.15	Cepheids
NGC 4214	2.93 ± 0.11	1.90 ± 0.03	9.12 ± 0.15	TRGB
NGC 4559	8.43 ± 0.66	2.08 ± 0.02	10.21 ± 0.27	TRGB
NGC 5005	18.37 ± 1.27	2.42 ± 0.04	11.09 ± 0.13	TRGB
NGC 5907	17.10 ± 0.71	2.33 ± 0.01	11.09 ± 0.10	TRGB
NGC 6503	6.25 ± 0.29	2.07 ± 0.01	9.97 ± 0.09	TRGB
NGC 6946	6.72 ± 0.50	2.20 ± 0.04	10.82 ± 0.28	TRGB
NGC 7331	13.90 ± 0.51	2.38 ± 0.01	11.14 ± 0.13	Cepheids
UGC01281	5.27 ± 0.24	1.74 ± 0.03	8.77 ± 0.06	TRGB
UGCA442	4.37 ± 0.20	1.75 ± 0.03	8.64 ± 0.06	TRGB

Table 3
Ponomareva et al. Cepheids/TRGB Calibrating Galaxies

Galaxy	D (Mpc)	log V_f (km s^{-1})	log M_b ($M_\odot$)	Distance Method
NGC 0253	3.56 ± 0.13	2.30 ± 0.01	10.72 ± 0.14	TRGB
NGC 0925	8.91 ± 0.28	2.06 ± 0.01	10.14 ± 0.10	Cepheids
NGC 1365	17.70 ± 0.81	2.33 ± 0.01	11.04 ± 0.13	Cepheids
NGC 2541	11.50 ± 0.47	2.00 ± 0.02	9.89 ± 0.07	Cepheids
NGC 3031	3.61 ± 0.09	2.33 ± 0.02	10.71 ± 0.14	Cepheids
NGC 3319	13.00 ± 0.53	2.05 ± 0.04	9.91 ± 0.08	Cepheids
NGC 3351	10.40 ± 0.28	2.25 ± 0.02	10.47 ± 0.14	Cepheids
NGC 3370	26.10 ± 0.72	2.18 ± 0.01	10.27 ± 0.13	Cepheids
NGC 3621	6.72 ± 0.18	2.16 ± 0.01	10.38 ± 0.09	Cepheids
NGC 3627	9.03 ± 0.29	2.26 ± 0.02	10.68 ± 0.14	Cepheids
NGC 4244	4.61 ± 0.19	2.04 ± 0.02	9.68 ± 0.09	TRGB
NGC 4258	7.31 ± 0.16	2.30 ± 0.01	10.72 ± 0.13	Cepheids
NGC 4414	17.80 ± 0.74	2.27 ± 0.02	10.80 ± 0.14	Cepheids
NGC 4535	16.10 ± 0.66	2.29 ± 0.01	10.69 ± 0.13	Cepheids
NGC 4536	14.60 ± 0.60	2.21 ± 0.03	10.47 ± 0.13	Cepheids
NGC 4605	5.54 ± 0.25	1.94 ± 0.02	9.52 ± 0.13	TRGB
NGC 4639	22.00 ± 0.71	2.27 ± 0.01	10.27 ± 0.14	Cepheids
NGC 4725	12.50 ± 0.46	2.33 ± 0.01	10.73 ± 0.14	Cepheids
NGC 5584	22.40 ± 0.72	2.12 ± 0.01	10.11 ± 0.13	Cepheids
NGC 7814	14.39 ± 0.50	2.34 ± 0.01	10.73 ± 0.11	TRGB
NGC 7793	3.58 ± 0.11	1.98 ± 0.04	9.62 ± 0.11	Cepheids

For the C/TRGB sample, observational error dominates the error budget compared to distance error in the M_b values. The observational error is 0.04 in log M_b whereas a 5% uncertainty to the C/TRGB distances contributes 0.05 in log M_b (V_f being independent of distance). Thus, the uncertainty in the y-axis of the bTFR is at most 0.06 in log M_b. And, if the slope is constant from sample to sample, the limit to our knowledge of the y intersect is limited by this error and the sample size.

2.4. The Baseline Baryonic Tully–Fisher Relation and the Flow SPARC Sample

With uncertainties from the previous section in mind, the maximum likelihood fit to the C/TRGB sample is shown as the solid line in Figure 1 (also listed in Table 1). This slope is consistent, within the errors, to the slope from Lelli et al. (2019, 3.85 versus 3.95 for the C/TRGB sample). For a mean error of 0.06 in log M_b and 0.02 in log V_f, the expected scatter for a slope of 3.95 is 0.050 in log–log space. The perpendicular residuals have a dispersion of 0.048, exactly what is expected for uncertainty solely from observational error and intrinsic scatter in Υ_*. Systematic model uncertainties are well mapped, and they are applied equally to all of the galaxies in the sample with only slight differences from low to high mass due to early-type morphology (i.e., bulge light) and additional molecular gas for high-mass galaxies. Their effects are more significant on the slope of the bTFR (as seen in Table 1), but will be irrelevant because our comparison samples will have the exact same corrections over the same range in galaxy mass.

In our 2016 study, we used a combination of redshift-independent distances, cluster distances, and Hubble flow distances (with an $H_o = 73\,\mathrm{km\,s^{-1}\,Mpc^{-1}}$) to calculate the baryonic masses. Since that study, the CosmicFlows-3 database has been released (Tully et al. 2019) with an improved flow model (Shaya et al. 2017). CosmicFlows-3 uses thousands of galaxies and clusters of galaxies to infer flow deviations from the cosmic expansion velocities owing to peculiar galaxy motions. The resulting dynamical model is then reversed with the knowledge of the observed redshift and position in the sky to deduce the true expansion velocity, which is then converted into distance using a particular H_o. For our analysis we use a subset of the inclination-selected SPARC sample of 125 galaxies where we have removed the 30 galaxies used for the C/TRGB calibration, leaving 95 galaxies with good CosmicFlows-3 or Virgo infall velocities (hereafter the flow SPARC sample).

There is a grouping in the flow SPARC data set of 26 galaxies at 18 Mpc that represents the Ursa Major cluster (Verheijen & Sancisi 2001), where we assumed all the Ursa Major galaxies to be at the mean cluster distance. In the interim, the CosmicFlows-3 project has assigned a mean distance of 17.2 Mpc for Ursa Major using the luminosity-based TF relation of 35 galaxies. We adopt this new distance for an $H_o = 75\,\mathrm{km\,s^{-1}\,Mpc^{-1}}$ with the caveat of adjusting this cluster distance for varying H_o values.

The slope of the maximum likelihood fit to the flow SPARC sample (using CosmicFlows-3 velocities; see Figure 2) is $x = 3.97 \pm 0.12$. The calibrating sample has an identical slope to the full sample, thus we feel confident in applying the fit from the C/TRGB galaxies as a baseline comparison for the full sample with varying H_o. In other words, we adopt the same slope of the C/TRGB sample and deduce H_o from the varying zero point on the flow SPARC sample.

Comparing the CosmicFlows-3 distance to the C/TRGB sample (for an $H_o = 75\,\mathrm{km\,s^{-1}\,Mpc^{-1}}$) finds a mean of zero and a standard deviation of 20% of the distance. The Virgo infall models (Mould et al. 2000) find similar means and

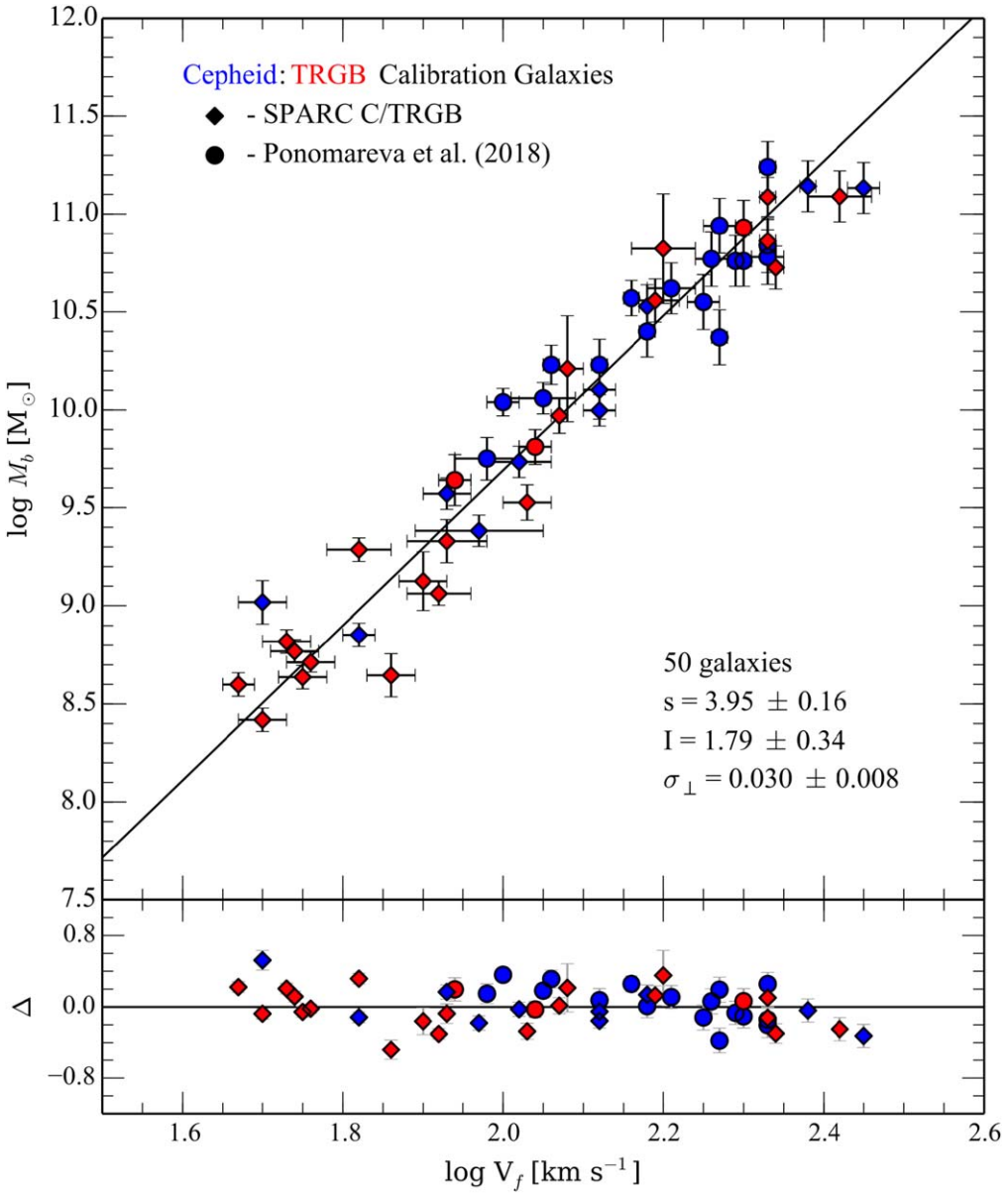

Figure 1. The bTFR diagram for 30 SPARC galaxies (diamond symbols) and 20 Ponomareva et al. (2018) disks (circular symbols) with C/TRGB distances. TRGB galaxies are marked in red, Cepheid galaxies in blue. The baryonic mass is the sum of the Spitzer 3.6 luminosity converted to stellar mass (see Schombert et al. 2019) and the total gas mass. The rotational velocity, V_f, is determined directly from H I rotation curves following the techniques outlined in Lelli et al. (2019). A maximum likelihood fit is shown and serves as the baseline slope and zero point for comparison to the flow SPARC sample of 95 galaxies.

dispersions. As the random errors in the C/TRGB distances are 5%, this implies most of the distance uncertainty is in the determination of the flow velocities on the level of 20%, in agreement with the uncertainty estimates from Tully et al. (2019). Given that the uncertainty in the baryon mass of the bTFR diagram is nearly twice that of the velocity axis, plus the distance errors will only map into the baryon mass, we then deduce that the dominant term for uncertainty for the flow SPARC sample is the combined observational errors to M_b plus distance error. The observational errors contribute 0.04 on log M_b where distance errors contribute as D^2 for 0.16 in log M_b. We assign a combined mean uncertainty of 0.20 in log for the baryon mass axis. Again, for a mean error of 0.20 in log M_b and 0.02 in log V_f, the expected scatter for a slope of 3.95 is 0.085 in log–log space. The perpendicular residuals have a dispersion of 0.067, slightly lower than what is expected for uncertainty solely from observational error. Using a slope of 3.97 lowered the dispersion by only a small amount to 0.065.

To explore the robustness of the derived H_o value, we repeat the linear fitting of the calibrating C/TRGB and the flow SPARC sample using three techniques. The first, used in Section 2.3, is the maximum likelihood technique considering the orthogonal intrinsic scatter. Here the intrinsic scatter is assumed to be Gaussian in the orthogonal direction to the fitted line. A second technique is to use the same maximum likelihood fit but with the intrinsic scatter in the vertical direction. Both fitting techniques are implemented in the BayesLineFit software available at the SPARC website. Lastly, we use a least trimmed squares technique (LTS; Cappellari et al. 2013) using the measured errors in M_b and V_f (the

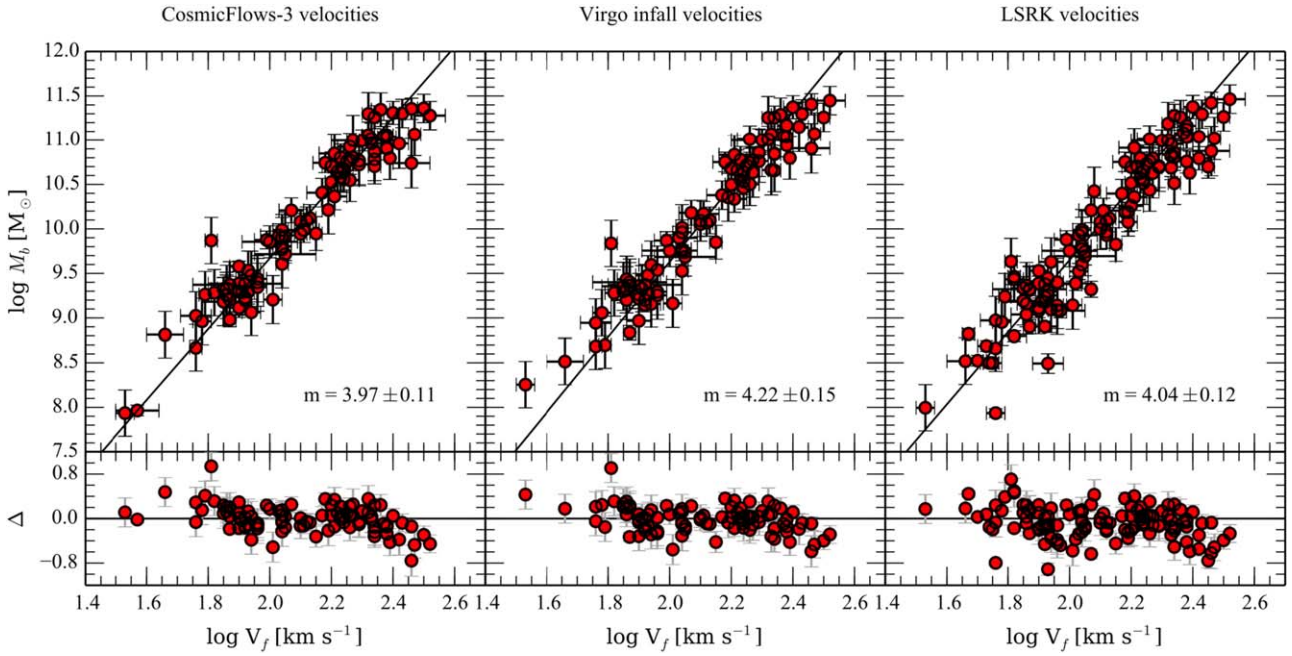

Figure 2. The bTFR for the flow SPARC galaxies with inclinations >30° and flat, outer rotation curves for highly accurate V_f values. The left panel displays the baryon masses calculated using the CosmicFlows-3 velocities. The solid line is the maximum likelihood fit. The center panel displays the baryon masses calculated for flow velocities based on a Virgo infall model from Mould et al. (2000). There is very little difference in the bTFR using either CosmicFlows-3 or Mould et al. velocities. The right panel displays the resulting bTFR using only local standard of rest (LSRK) velocities. While similar to the infall distances, the scatter is 15% larger, from which we conclude that LSRK velocities are inadequate to deduce H_o. The residuals in M_b from the C/TRGB fit are shown in the bottom panels. The flow model fits are listed in Table 5.

Table 4
C/TRGB Fitting Results

log A	x	ΔH_o	Fit
1.78 ± 0.35	3.95 ± 0.17	···	ML orthogonal
2.29 ± 0.31	3.71 ± 0.15	−0.3	ML vertical
2.34 ± 0.03	3.69 ± 0.12	−1.0	LTS

Table 5
Flow SPARC Fits

x	H_o	Flow Model
3.97 ± 0.11	75.1 ± 2.3	CosmicFlows-3
4.22 ± 0.15	74.6 ± 2.4	Virgo Infall
4.01 ± 0.11	77.5 ± 2.4	Virgo+GA Infall
4.04 ± 0.12	72.8 ± 2.7	LSRK

Appendix of Lelli et al. 2019 discusses the mathematical and statistical properties of these methods and provide basic comparisons).

The results for the three fitting techniques are shown in Table 4. While the ML vertical and LTS fits display shallower slopes, the slopes are consistent between the calibrating C/TRGB and flow SPARC samples (in other words, larger and different samples produce the same trends between orthogonal, vertical, and LTS). Slightly different midpoints to the fits will result in a systematic variation in the deduced H_o values from the orthogonal fit as shown in the table as ΔH_o. Even though the uncertainties are greater in the vertical direction, we believe the orthogonal fits are more representative of the data and the non-negligible error in V_f. We can assign a systematic error of ±0.5 to the fitting methods.

3. Results

The bTFR for the flow SPARC sample (95 galaxies) is shown in Figure 2 using the CosmicFlows-3 velocities (left panel), the Virgo infall flow model (Mould et al. 2000, center panel), and only the LSRK velocities (galactocentric velocity, right panel). There is very little difference in the distribution using CosmicFlows-3 versus Virgo infall velocities. The derived Virgo infall slope is 4.22, compared to 3.97 for the CosmicFlows-3 values, which is primarily due to the fact that the flow corrections are small for a majority of the SPARC sample. The LSRK galactic center velocities have a similar slope (4.04), but with 15% more scatter and the loss of five galaxies with negative redshifts.

We conclude that distance uncertainties are identical in either method of correcting for local infall to the observed redshifts and we use the CosmicFlows-3 velocities for our final conclusions. Using a C/TRGB slope of 3.95, the calibrating and flow SPARC samples have similar dispersions around that zero point. In other words, the two samples, with identical sources of error in their kinematics and photometry, produce nearly identical slopes to the bTFR whether using redshift-independent C/TRGB distances or CosmicFlows-3 velocities.

A uniform change in the distance model (i.e., H_o) will produce a linear shift from the C/TRGB bTFR (upward for larger distances) such that the bTFR can be used as a distance scale indicator much like the luminous TF or the Fundamental Plane relation. In other words, one can reproduce the C/TRGB bTFR zero point with the appropriate H_o to convert redshifts into distance to apply to 3.6 luminosities and H I fluxes to determine the baryon mass. Comparing the residuals along the M_b axis with the linear fit to the C/TRGB sample becomes a simple t-test. In this case, the empirical correlation of the bTFR

is stronger (less scatter) than the Fundamental Plane. In addition, errors in the distance apply to each galaxy, rather than a cluster or group uncertainty as with many traditional applications of the luminous TF relation. So, increasing the sample size has a notable effect on the scatter versus adding a new galaxy cluster to the luminous TF relation.

A formal match from the C/TRGB bTFR to the flow SPARC sample using CosmicFlows-3 velocities produces $H_o = 75.1 \pm 2.3\,\mathrm{km\,s^{-1}\,Mpc^{-1}}$ using the maximum likelihood orthogonal fitting method. This result is relatively independent of bTFR slope and/or flow model. Slight changes in the slope (for example, from 3.9 to 4.1) only widens the dispersion of the residuals from the bTFR, and the differences between the different distance samples operate only along the M_b axis. The use of a slope of 3.8 or 4.1 (the range from the luminous TF relation) has no effect on the mean normalization and would only increase the error on H_o by 0.5%. Likewise, as can be seen in Figure 2, using the Virgo infall flow model produces a nearly identical bTFR fit to the CosmicFlows-3 bTFR (and an $H_o = 74.6\,\mathrm{km\,s^{-1}\,Mpc^{-1}}$).

Of the calibrating sample of 50 galaxies, 23 are TRGB galaxies and any zero-point errors would enter through errors in the TRGB method. The estimated uncertainty on M_{814}^{TRGB} is 0.022 (stat) and 0.039 (sys) (primarily through uncertainty to the distance to the LMC; Riess 2019). As a numerical experiment, we allowed the zero point for the TRGB galaxies to shift upward and downward by 0.05 mag then refit the bTFR for the C/TRGB sample. The results are shown in Table 1. Due to the fact that 27 of the 50 galaxies in the C/TRGB sample uses Cepheids as a distance indicator, the effect on the C/TRGB bTFR is small, only ±0.3 (sys) in the determination of H_o. In a similar fashion, we examined the effect of different fitting methods of the C/TRGB sample. This procedure was discussed in Section 2.4, and we adopt a systematic error in the fitting methods of ±0.5 (sys).

Comparison of the flow models to C/TRGB galaxies finds all of the expected distances to be within 1σ of C/TRGB distances with similar dispersions of 20%. We find CosmicFlows-3 to be the closest match to the C/TRGB distances followed by the simple Virgo infall then the Virgo plus Great Attractor (Virgo+GA) correction. The Virgo + Great Attractor + Shapley supercluster produced the same results as the Virgo +GA model. As not applying infall corrections raises the scatter by 15%–20%, we find, unsurprisingly, that the LSRK values do not represent the correct value of H_o. In addition, the slope of the bTFR from orthogonal fits using the CosmicFlows-3 velocities is closer to the C/TRGB bTFR slope than using any of the Virgo infall models. For this reason, we adopt the CosmicFlows-3 model and the orthogonal fits for our conclusions.

Using the Virgo infall model consistently finds an H_o value $0.4\,\mathrm{km\,s^{-1}\,Mpc^{-1}}$ lower than the value found from CosmicFlows-3 velocities across all three fitting methods. Using the Virgo+GA and Virgo+GA+Shapley infall models consistently finds H_o values greater than the baseline by $2.4\,\mathrm{km\,s^{-1}\,Mpc^{-1}}$. No correction for peculiar velocities (LSRK) consistently finds H_o values $2.5\,\mathrm{km\,s^{-1}\,Mpc^{-1}}$ lower than the CosmicFlows-3 values. The standard deviation between the various flow models is found to be $1.5\,\mathrm{km\,s^{-1}\,Mpc^{-1}}$, which we adopt as the systematic variation for our flow model. As this value dominates the other systematics in the fitting methods or zero-point errors, we use this value to indicate the expected systematic uncertainty in our measurements. Thus, we adopt a formal fit to the flow SPARC data set of $H_o = 75.1 \pm 2.3$ (stat) ± 1.5 (sys) $\mathrm{km\,s^{-1}\,Mpc^{-1}}$.

To test the significance level of the orthogonal fit to competing values of H_o, we recalculate the flow SPARC sample baryonic masses using distances given by $H_o = 67.4\,\mathrm{km\,s^{-1}\,Mpc^{-1}}$. This is the value of H_o found by the Planck mission (Planck Collaboration et al. 2016) fitting CMB anisotropies with the base ΛCDM cosmology. The resulting bTFRs are shown in Figure 3 (residuals in the bottom panel). Assuming the linear fit to the calibrating C/TRGB sample (shown as a solid line in Figure 3), we can perform a simple t-test analysis on the distribution of perpendiculars from the linear fit. For the C/TRGB $H_o = 75.1\,\mathrm{km\,s^{-1}\,Mpc^{-1}}$ and $H_o = 67.4\,\mathrm{km\,s^{-1}\,Mpc^{-1}}$ samples we have, respectively, mean perpendiculars of 0.0 (by definition), −0.001, and −0.024 with standard deviations of 0.057 for the calibrating sample and 0.069 for the H_o samples. The C/TRGB and $H_o = 75.1\,\mathrm{km\,s^{-1}\,Mpc^{-1}}$ samples are in agreement at a high level, the $H_o = 67.4\,\mathrm{km\,s^{-1}\,Mpc^{-1}}$ sample is rejected at the 99.98% level. In fact, all values of H_o below 70.5 are rejected at the 95% level.

4. Conclusions

As outlined in the Introduction, the bTFR is one of the strongest empirical correlations in extragalactic astronomy. While there exist many other correlations between galaxy characteristics with similar scatter (such as scaling relations between effective radius and surface brightness in ellipticals; see Schombert 2017), other galaxy correlations often involve coupled parameters measured by a similar procedure (e.g., photometry). The bTFR involves two distinct parameters, rotation velocity and baryonic mass, both measured by independent methods (H I observations provide both the H I mass and the rotation velocities, but the former comes from the total intensity map and the latter from the velocity map, so they are effectively independent observables). With the advent of accurate rotation curves, the determination of V_f has very little uncertainty and is mapped to the very edge of the baryonic extent of a galaxy. In addition, the behavior of V_f with respect to past measures of rotation velocity is now well known (see Ponomareva et al. 2018; Lelli et al. 2019).

Likewise, the use of near-IR luminosities to determine the stellar mass component of the baryonic mass has minimized the largest source of uncertainty on that axis of the bTFR, the value of Υ_* (see Zaritsky et al. 2014). The error budget in M_b, as applied to as a new distance indicator, is now dominated by the observational error in the H I fluxes and 3.6 photometry, which approaches 10% each. This means the baryonic mass, which is obtained without reference to kinematics, is determined to a higher degree of accuracy than could be obtained simply from the kinematics. The error on this axis is completely dominated by uncertainty in distance, which in turn makes it an ideal distance scale indicator when calibrated with redshift-independent samples. Our analysis herein results in a high value of H_o near $75\,\mathrm{km\,s^{-1}\,Mpc^{-1}}$.

It is becoming increasingly obvious that values of H_o, determined from empirical astronomical correlations differ significantly from values determined from expectations estimated by cosmological model fits (e.g., fits to the angular power spectrum of the CMB fluctuations). There is a long

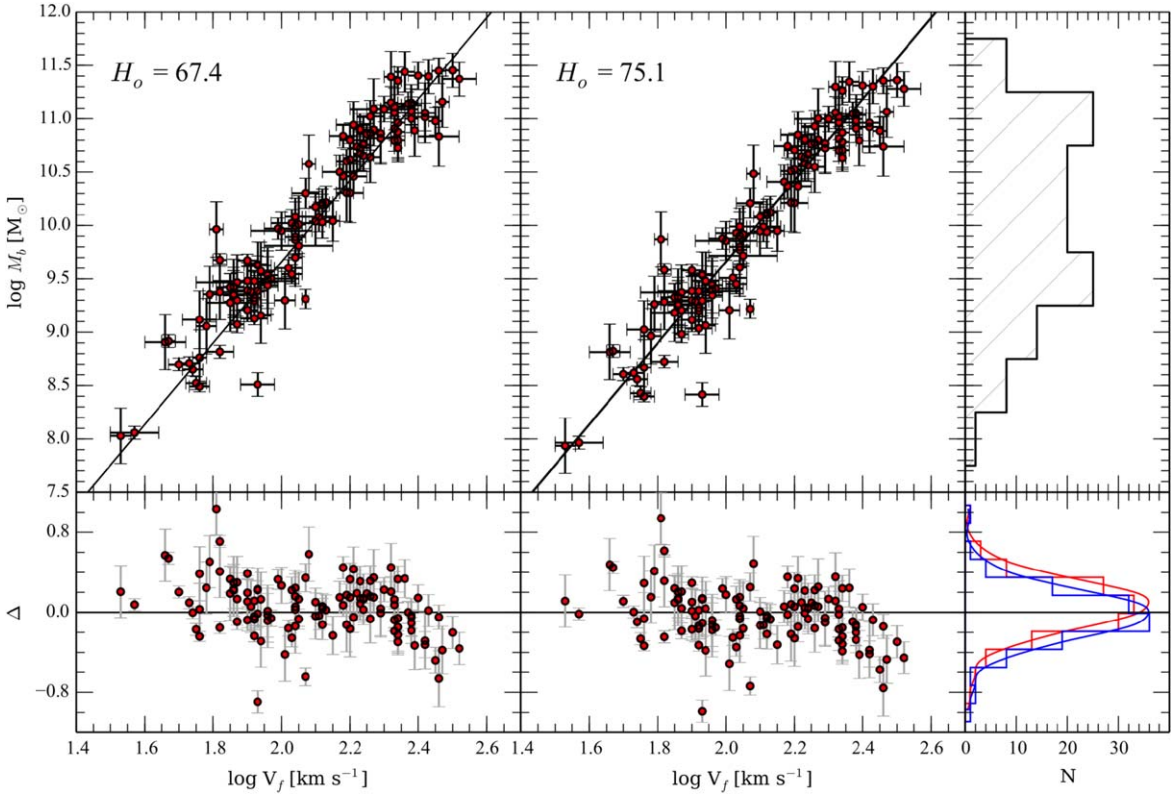

Figure 3. The bTFR for the flow SPARC galaxies, using CosmicFlows-3 velocities, with a $H_o = 67.4$ km s^{-1} Mpc^{-1} (left panel) and $H_o = 75.1$ km s^{-1} Mpc^{-1} (right panel). The solid line is the baseline fit from Figure 1. Residuals are plotted in the bottom panels. Histograms of the range in M_b and residuals are shown on the right (blue for 75.1, red for 67.4). As V_f is independent of distance, changing H_o has the effect of increasing the baryon mass by ΔH_o^2. H_o values less than 70.5 are ruled out at the 95% confidence level.

history in observational astronomy of constructing a distance scale to determine the local H_o independent of any underlying astrophysics. In fact, the best techniques rely on as little modeling as possible. Where model values are used (for example, Υ_* in determining stellar mass from 3.6 luminosities), those values are highly constrained by limits based on knowledge of galaxy colors and past SFRs.

However, one cannot ignore that the model fits to the CMB under a ΛCDM cosmology have been extremely successful at explaining the details of these observations of the early universe. For example, the concordance ΛCDM model is in agreement with measurements of anisotropies in the temperature and polarization of the CMB (Planck Collaboration et al. 2016) as well as fluctuations in the baryonic acoustic oscillations (Alam et al. 2017). The temperature and polarization anisotropy spectra are well fit by a six-parameter model that does not give a direct measurement of H_o, but provide an inferred value of 67.4 ± 0.5 km s^{-1} Mpc^{-1}.

An important distinction is that observations of the CMB do not measure H_o directly, but rather predict what the value of H_o should be given a specific model of the expanding universe with cosmological parameters in a ΛCDM framework. This framework also makes predictions on the power spectrum, polarization, and anisotropies (also expressed through various cosmological parameters). The actual measured values of H_o, through distance ladder techniques, do not agree with this deduced value.

In this study, we present another empirical method to deduce H_o. We calibrate the bTFR using 50 galaxies with Cepheid and/or TRGB distances and apply this relation to another 95 galaxies from the SPARC sample to deduce the value of H_o. Due to the nature of the observations, only the baryonic mass axis is sensitive to distance. Leveraging the fit to the redshift-independent calibrators, we find that $H_o = 75.1$ km s^{-1} Mpc^{-1}, ruling out all values below 70 with a 95% degree of confidence.

High values of H_o near 75 km s^{-1} Mpc^{-1} continue to be more appropriate when involving empirical, observational issues of galaxy distance, while lower values of H_o are required for the framework that involves the CMB and the physics of the early universe. These are, in a real sense, separate chains of deductive reasoning. And, while in a rule-driven universe H_o should be connected from the early universe to today, there exist many explanations that do not require that to be true (Verde et al. 2019). In addition, there is increasing reason to doubt the CDM paradigm on galaxy scales (see McGaugh et al. 2016; Bullock & Boylan-Kolchin 2017) despite its success on cosmological scales

The future use of the bTFR as a distance indicator is encouraging due to the fact that the intrinsic bTFR scatter in the C/TRGB sample and the flow SPARC sample are similar, despite the difference in sample size. This indicates that additional calibrating galaxies will significantly improve the slope and zero point to the bTFR while additional flow galaxies will severely push down both random and systematic errors. In fact, the current dominating systematic uncertainty (± 1.5 km s^{-1} Mpc^{-1}) depends on how the 95 flow SPARC galaxies sample specific regions of the nearby universe, where flow velocities can differ by more than the mean global difference from different flow models (e.g., CosmicFlows-3 versus Virgo Infall). Additional flow galaxies will allow us to

sample a larger volume of the nearby universe, where different flow models have, on average, smaller differences.

We thank Brent Tully and an anonymous referee for comments to improve the text. Software for this project was developed under NASA's AIRS and ADAP Programs. This work is based in part on observations made with the Spitzer Space Telescope, which is operated by the Jet Propulsion Laboratory, California Institute of Technology under a contract with NASA. Support for this work was provided by NASA through an award issued by JPL/Caltech. Other aspects of this work were supported in part by NASA ADAP grant NNX11AF89G and NSF grant AST 0908370. As usual, this research has made use of the NASA/IPAC Extragalactic Database (NED) which is operated by the Jet Propulsion Laboratory, California Institute of Technology, under contract with the National Aeronautics and Space Administration.

ORCID iDs

James Schombert https://orcid.org/0000-0003-2022-1911
Stacy McGaugh https://orcid.org/0000-0002-9762-0980
Federico Lelli https://orcid.org/0000-0002-9024-9883

References

Alam, S., Zhu, H., Croft, R. A. C., et al. 2017, MNRAS, 470, 2822
Aubourg, É, Bailey, S., Bautista, J. E., et al. 2015, PhRvD, 92, 123516
Bell, E. F., McIntosh, D. H., Katz, N., et al. 2003, ApJS, 149, 289
Bhardwaj, A., Kanbur, S. M., Macri, L. M., et al. 2016, AJ, 151, 88
Bradford, J. D., Geha, M. C., & Blanton, M. R. 2015, ApJ, 809, 146
Bullock, J. S., & Boylan-Kolchin, M. 2017, ARA&A, 55, 343
Cappellari, M., Scott, N., Alatalo, K., et al. 2013, MNRAS, 432, 1709
Dutton, A. A. 2012, MNRAS, 424, 3123
Freedman, W. L., Madore, B. F., Hatt, D., et al. 2019, ApJ, 882, 34
Freeman, K. C. 1999, Ap&SS, 269, 119
Gnedin, N. Y. 2012, ApJ, 754, 113
Iorio, G., Fraternali, F., Nipoti, C., et al. 2017, MNRAS, 466, 4159
Lelli, F., McGaugh, S. S., & Schombert, J. M. 2016a, ApJL, 816, L14
Lelli, F., McGaugh, S. S., & Schombert, J. M. 2016b, AJ, 152, 157
Lelli, F., McGaugh, S. S., Schombert, J. M., et al. 2019, MNRAS, 484, 3267
Li, P., Lelli, F., McGaugh, S., et al. 2020, ApJS, 247, 31
McGaugh, S. S. 2012, AJ, 143, 40
McGaugh, S. S., Lelli, F., & Schombert, J. M. 2016, PhRvL, 117, 201101
McGaugh, S. S., Lelli, F., & Schombert, J. M. 2020, RNAAS, 4, 45
McGaugh, S. S., & Schombert, J. M. 2015, ApJ, 802, 18
McGaugh, S. S., Schombert, J. M., Bothun, G. D., et al. 2000, ApJL, 533, L99
Meidt, S. E., Schinnerer, E., van de Ven, G., et al. 2014, ApJ, 788, 144
Mould, J. R., Huchra, J. P., Freedman, W. L., et al. 2000, ApJ, 529, 786
Planck Collaboration, Ade, P. A. R., Aghanim, N., et al. 2016, A&A, 594, A13
Ponomareva, A. A., Verheijen, M. A. W., Papastergis, E., et al. 2018, MNRAS, 474, 4366
Portinari, L., Sommer-Larsen, J., & Tantalo, R. 2004, in IAU Symp. 220, Dark Matter in Galaxies, ed. S. D. Ryder et al. (San Fransisco, CA: ASP), 309
Qu, Z., & Bregman, J. N. 2019, ApJ, 880, 89
Riess, A. G. 2019, NatRP, 2, 10
Riess, A. G., Macri, L. M., Hoffmann, S. L., et al. 2016, ApJ, 826, 56
Sakai, S., Zaritsky, D., & Kennicutt, R. C. 2000, AJ, 119, 1197
Schombert, J., Maciel, T., & McGaugh, S. 2011, AdAst, 2011, 143698
Schombert, J., & McGaugh, S. 2014, PASA, 31, e036
Schombert, J., McGaugh, S., & Lelli, F. 2019, MNRAS, 483, 1496
Schombert, J. M. 2017, PASA, 34, e016
Shaya, E. J., Tully, R. B., Hoffman, Y., et al. 2017, ApJ, 850, 207
Sorce, J. G., Courtois, H. M., Tully, R. B., et al. 2013, ApJ, 765, 94
Tully, R. B., Courtois, H. M., Dolphin, A. E., et al. 2013, AJ, 146, 86
Tully, R. B., & Fisher, J. R. 1977, A&A, 500, 105
Tully, R. B., Pomarède, D., Graziani, R., et al. 2019, ApJ, 880, 24
Verde, L., Treu, T., & Riess, A. G. 2019, NatAs, 3, 891
Verheijen, M. A. W. 2001, ApJ, 563, 694
Verheijen, M. A. W., & Sancisi, R. 2001, A&A, 370, 765
Zaritsky, D., Courtois, H., Muñoz-Mateos, J.-C., et al. 2014, AJ, 147, 134